the strong gravitational bending of light rays[9]. Thus, it is very likely that VLBI observations of Sgr A* at 1 mm or shorter will reach the region comparable to its shadow, which can be used to differentiate between the SMBH scenario and other supermassive non-baryonic stars[4,21].

The two-point fit to the well determined intrinsic sizes at 7 and 3.5 mm shows a λ^{β}-dependence of the intrinsic source size with $\beta = 1.09^{+0.34}_{-0.32}$ (Fig. 2). Also plotted in Fig. 2 are two inferred lower limits of 0.02 and 0.008 mas to the intrinsic size at 1.3 and 0.8 mm, respectively, from the absence of refractive scintillation[22]. These lower limits are consistent with the extrapolation of the λ^{β}-dependence. However, we note that these two lower limits are only about 2 and 0.8 $R_{\rm s.s.o}$ which are smaller than the last stable orbit (LSO) radius of $3R_{\rm sch}$ for a non-rotating (Schwarzschild) black hole. There is some evidence that Sgr A* is a rotating black hole[23]. For a prograde maximally rotating Kerr black hole, the LSO radius is $0.5R_{\rm sch}$. The LSO establishes the lower limit to the emission region size. Hence the λ^{β}-dependence will eventually reach a minimum. As such, the turn-over frequency[24] seen in the entire spectrum of Sgr A* might tell us the smallest size of the emission, which can be further used to constrain its spin, if any.

The extrapolated intrinsic size at 1.35 cm is $0.555^{+0.176}_{-0.115}$ mas. This, when compared to the scattering angle of 2.576 ± 0.036 mas, is consistent with the idea that the scattering effect dominates the observed source size at 1.35 cm. This deduced source size is also formally consistent with the reported detection of $0.726^{+0.152}_{-0.111}$ mas, to within the uncertainties[6].

The derived $\lambda^{1.09}$-dependence requires that the emission at different wavelengths is dominated by different emitting regions, and thus conclusively excludes those models without the stratified emission structure. Along with the detected intrinsic major axis size, we can derive a lower limit to the intrinsic brightness temperature as $T_{\rm b} \geq 1.36 \times 10^9 \times^{S_\lambda \lambda^2}_{\Theta^{\rm ma}_{\rm int}\Theta^{\rm mi}_{\rm int}}$ K; here S_λ is the flux density in Jy at wavelength λ in cm, and $\Theta^{\rm ma,mi}_{\rm int}$ is the intrinsic major axis size in mas. There is a wavelength dependence of the lower limit $T_{\rm b}$ as $\lambda^{-\alpha-0.18}$ (assuming $S_\lambda \propto \lambda^{-\alpha}$). Using the flux densities of 1.0 and 1.2 Jy at 7 and 3.5 mm, respectively, the corresponding minimal $T_{\rm b}$ is 0.9×10^{10} and 1.2×10^{10} K, greater than the prediction of the spherical accretion model[25]. However, this lower limit of 10^{10} K, and the spatial distribution of the radio emission, can be explained easily by the inhomogeneous jet model[26,27], in which the magnetic field and the electron number density vary with the distance (r) to the origin of the jet as r^{-1} and r^{-2}, respectively. On the other hand, the radiatively inefficient accretion flow (RIAF) model of Sgr A* (ref. 28) can also account for a brightness temperature of $>10^{10}$ K as well as the observed spectral energy distribution. The prediction of $\lambda^{0.9}$ from the hybrid thermal-nonthermal synchrotron radiation from RIAF (ref. 29) is in agreement with the estimated $\lambda^{1.09^{+0.11}_{-0.13}}$ relation. Here, the possible existence of strong outflows from the accretion disk was not taken into account. To further discern between them, it is important to study the correlation between the detected X-ray variability and the variations frequently seen in the radio to sub-millimetre wavelengths, which would yield further information on the intrinsic density structure of the emitting zone.

Received 1 July; accepted 31 August 2005.

1. Begelman, M. C. Evidence for black holes. *Science* **300**, 1898–1903 (2003).
2. Kormendy, J. & Richstone, D. Inward bound–The search for supermassive black holes in galactic nuclei. *Annu. Rev. Astron. Astrophys.* **33**, 581–624 (1995).
3. Rees, M. J. Black hole models for active galactic nuclei. *Annu. Rev. Astron. Astrophys.* **22**, 471–506 (1984).
4. Backer, B. & Brown, R. L. Intense sub-arcsecond structure in the Galactic Center. *Astrophys. J.* **194**, 265–270 (1974).
5. Melia, F. & Falcke, H. The supermassive black hole at the Galactic Center. *Annu. Rev. Astron. Astrophys.* **39**, 309–352 (2001).
6. Schödel, R. *et al.* A star in a 15.2 year orbit around the supermassive black hole at the centre of the Milky Way. *Nature* **419**, 694–696 (2002).
7. Ghez, A. M. *et al.* Stellar orbits around the Galactic Center black hole. *Astrophys. J.* **620**, 744–757 (2005).
8. Bower, G. C. *et al.* Detection of the intrinsic size of Sagittarius A* through closure amplitude imaging. *Science* **304**, 704–708 (2004).
9. Falcke, H., Melia, F. & Agol, E. Viewing the shadow of the black hole at the Galactic Center. *Astrophys. J.* **528**, L13–L16 (2000).
10. Shen, Z.-Q. & Lo, K. Y. High-resolution 86 GHz VLBA imaging of Sgr A*. *Prog. Theor. Phys. Suppl.* **155**, 413–414 (2004).
11. Reid, M. *et al.* The position, motion, and mass of Sgr A*. *Astron. Nachr.* **324** (Suppl. Iss. 1), 505–511 (2003).
12. Davies, R. D., Walsh, D. & Booth, R. S. The radio source at the Galactic nucleus. *Mon. Not. R. Astron. Soc.* **177**, 319–333 (1976).
13. Lo, K. Y. *et al.* On the size of the galactic centre compact radio source diameter <20 AU. *Nature* **315**, 124–126 (1985).
14. Alberdi, A. *et al.* VLBA Image of Sgr A* at $\lambda = 1.35$ cm. *Astron. Astrophys.* **277**, L1–L4 (1993).
15. Bower, G. C. & Backer, D. C. 7 Millimeter VLBA observations of Sagittarius A*. *Astrophys. J.* **496**, L97–100 (1998).
16. Lo, K. Y., Shen, Z.-Q., Zhao, J.-H. & Ho, P. T. P. Intrinsic size of Sagittarius A*: 72 Schwarzschild radii. *Astrophys. J.* **508**, L61–L64 (1998).
17. Shen, Z.-Q., Liang, M. C., Lo, K. Y. & Miyoshi, M. Searching for structural variability in Sgr A*. *Astron. Nachr.* **324** (Suppl. Iss. 1), 383–389 (2003).
18. Doeleman, S. S. *et al.* Structure of Sagittarius A* at 86 GHz using VLBI closure quantities. *Astron. J.* **121**, 2610–2617 (2001).
19. Miyoshi, M. *et al.* Evidence for a black hole from high rotation velocities in a sub-parsec region of NGC4258. *Nature* **373**, 127–129 (1995).
20. Maoz, E. Dynamical constraints on alternatives to supermassive black holes in galactic nuclei. *Astrophys. J.* **494**, L181–L184 (1998).
21. Torres, D. F., Capozziello, S. & Lambiase, G. Supermassive boson star at the galactic center? *Phys. Rev. D* **62**, 104012 (2000).
22. Gwinn, C. R., Danen, R. M., Tran, T. Kh., Middleditch, J. & Ozernoy, L. M. The Galactic center radio source shines below the Compton limit. *Astrophys. J.* **381**, L43–L46 (1991).
23. Genzel, R. *et al.* Near-infrared flares from accreting gas around the supermassive black hole at the Galactic Centre. *Nature* **425**, 934–937 (2003).
24. Falcke, H. *et al.* The simultaneous spectrum of Sagittarius A* from 20 centimeter to 1 millimeter and the nature of the millimeter excess. *Astrophys. J.* **499**, 731–734 (1998).
25. Melia, F. An accretion black hole model for Sagittarius A*. II. A detailed study. *Astrophys. J.* **426**, 577–585 (1994).
26. Königl, A. Relativistic jets as X-ray and gamma-ray sources. *Astrophys. J.* **243**, 700–709 (1981).
27. Falcke, H. & Markoff, S. The jet model for Sgr A*: Radio and X-ray spectrum. *Astron. Astrophys.* **362**, 113–118 (2000).
28. Yuan, F., Quataert, E. & Narayan, R. Nonthermal electrons in radiatively inefficient accretion flow models of Sagittarius A*. *Astrophys. J.* **598**, 301–312 (2003).
29. Özel, F., Psaltis, D. & Narayan, R. Hybrid thermal-nonthermal synchrotron emission from hot accretion flows. *Astrophys. J.* **541**, 234–249 (2000).

Supplementary Information is linked to the online version of the paper at www.nature.com/nature.

Acknowledgements The Very Large Array and the Very Long Baseline Array are operated by the National Radio Astronomy Observatory, which is a facility of the National Science Foundation, operated under cooperative agreement by Associated Universities Inc. Z.-Q.S. acknowledges support from the One-Hundred-Talent programme of the Chinese Academy of Sciences.

Author Information Reprints and permissions information is available at npg.nature.com/reprintsandpermissions. The authors declare no competing financial interests. Correspondence and requests for materials should be addressed to Z.-Q.S. (zshen@shao.ac.cn).

LETTERS

Active control of slow light on a chip with photonic crystal waveguides

Yurii A. Vlasov[1], Martin O'Boyle[1], Hendrik F. Hamann[1] & Sharee J. McNab[1]

It is known that light can be slowed down in dispersive materials near resonances[1]. Dramatic reduction of the light group velocity—and even bringing light pulses to a complete halt—has been demonstrated recently in various atomic[2–4] and solid state systems[5–8], where the material absorption is cancelled via quantum optical coherent effects[4–6,7]. Exploitation of slow light phenomena has potential for applications ranging from all-optical storage to all-optical switching[8,10]. Existing schemes, however, are restricted to the narrow frequency range of the material resonance, which limits the operation frequency, maximum data rate and storage capacity[10]. Moreover, the implementation of external lasers, low pressures and/or low temperatures prevents miniaturization and hinders practical applications. Here we experimentally demonstrate an over 300-fold reduction of the group velocity on a silicon chip via an ultra-compact photonic integrated circuit using low-loss silicon photonic crystal waveguides[11,12] that can support an optical mode with a submicrometre cross-section[13,14]. In addition, we show fast (~100 ns) and efficient (2 mW electric power) active control of the group velocity by localized heating of the photonic crystal waveguide with an integrated micro-heater.

The propagation of light pulses in a dielectric medium with refractive index $n(\lambda)$ is described by the group velocity, defined as $V_g = c/(n - \lambda {\rm d}n/{\rm d}\lambda) = c/n_g$, where c is the speed of light in vacuum, n is the phase refractive index, λ is the wavelength, and n_g is the group index. When dispersion is negative and large ($|{\rm d}n/{\rm d}\lambda| \ll 0$), the pulses can be significantly delayed with respect to free space propagation. Slow group velocity was measured recently in photonic crystal structures with ultrafast pulse propagation techniques[15,16]. Surface coupling to slow light modes was also inferred from the absence of transmission of light at wavelengths corresponding to strong dispersion[17,18]. However, the accuracy of the group velocity determination in both of these approaches is limited, as they are relying heavily on measurements of the amplitude of the transmitted light, whereas the dispersion is inherently connected with its phase. For example, significant amplitude reshaping of short optical pulses owing to strong group velocity dispersion makes the group delay assignment progressively inaccurate[15] in the slow group velocity regime. In contrast, phase-sensitive optical techniques based on observation of interference fringes in transmission spectra were successfully used to accurately measure group indices approaching 100 (refs 14, 19). To utilize this interferometric approach, we designed and fabricated an integrated Mach–Zehnder interferometer (MZI) employing photonic crystal waveguides.

Silicon photonic crystal waveguides used in our experiments are shown in Fig. 1. These are resonant photonic structures formed by etching a periodic array (periodicity $a = 437$ nm) of holes with radius 0.25a in a 223-nm-thick silicon suspended membrane. The light is coupled to the photonic crystal waveguide through a polymer-based fibre coupler and single-mode access strip waveguide butt-coupled to the photonic crystal[11]. Details of the structural parameters and device fabrication are described in Methods. The utilization of laterally tapered spot-sized converters and careful termination of the photonic crystal lattice[20] at a position half way through the holes nearest to the waveguide (see Fig. 1a) allows efficient coupling to the

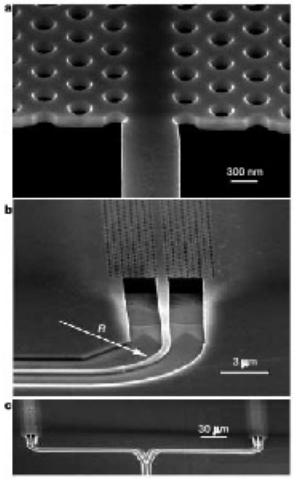

Figure 1 | SEM images of a passive unbalanced Mach–Zehnder interferometer using photonic crystal waveguides. a, Input section of the photonic crystal waveguide showing the suspended silicon membrane etched with holes and butt-coupled to a strip waveguide. The termination of the photonic crystal lattice at the coupling interface is chosen to obtain highest coupling efficiency in the slow light regime. **b**, Broader view of the photonic crystal waveguide membrane and input strip waveguide. After passing through a sharp 90° bend with radius $R = 5\,\mu$m, the mode is widened in the tapered section to better match the photonic crystal slow light mode. **c**, View of the input of the Mach–Zehnder interferometer (MZI) with reference (left) and signal (right) arms and a compact 15° angle Y-junction that splits the light equally between the arms. The output side of the optical circuit has an analogous Y-junction and is terminated by a single output strip waveguide.

[1]IBM T.J. Watson Research Center, Yorktown Heights, New York 10598, USA.

slow light mode. A typical transmission spectrum of a straight photonic crystal waveguide of 250 μm length is shown in Fig. 2a (black curve). According to photonic band structure calculations performed with a plane wave expansion method[20] (black dashed curve in Fig. 2b, see also Methods), the group index becomes increasingly large within a 20 nm bandwidth around 1,620 nm in the vicinity of the sharp cut-off of the TE-like waveguiding mode.

In order to measure the group velocity interferometrically, an integrated unbalanced MZI with a footprint of only 0.04 mm^2 was designed (Fig. 1c). The light is divided equally at the compact 15°-angle Y-splitter and is passed through two almost identical photonic crystal waveguides (Fig. 1c) with a small but noticeable difference in the hole radii of $0.251a$ (reference arm) and $0.263a$ (signal arm). Increasing the hole radii in the signal arm shifts the photonic crystal mode cut-off by approximately 20 nm to shorter wavelengths at around 1,600 nm. In the spectral region of interest (between 1,500 nm and 1,600 nm), the group index in the reference arm can be considered almost constant, $n_g^{ref} \approx 5$ (see dashed black curve in Fig. 2b), while the group index of the signal arm $n_g^{sig}(\lambda)$ exhibits a strong increase. Correspondingly, when the light from both arms is recombined at the output Y-coupler of the MZI, strong cosine-like interference fringes with a modulation depth exceeding 25 dB are observed in the transmission spectrum (red curve in Fig. 2a). The fringes converge towards the cut-off of the photonic crystal mode in the signal arm at around 1,600 nm. The spectral distance between corresponding minima and maxima significantly decreases from 20 nm at 1,510 nm to numbers of the order of 0.01 nm around 1,602.8 nm, reflecting a sharp increase in the relative phase shift. Approaching the cut-off of the signal arm, the fringe visibility decreases sharply from ~25 dB to ~2 dB, indicating significant wavelength dependent losses in the circuit. The transmission above 1,602.8 nm is provided only by the reference arm up to the cut-off wavelength of that arm around 1,620 nm.

The maxima and minima of the oscillations correspond to constructive and destructive interference, respectively, with the relative phase shift between two adjacent extrema equal to π. The spectral dependence of the group index in the signal arm can then be deduced from positions of corresponding minima λ_{min} and maxima λ_{max} as $n_g^{sig}(\lambda) = \lambda_{min}\lambda_{max}/[2L(\lambda_{min} - \lambda_{max})] + n_g^{ref}(\lambda)$, where $L = 250$ μm is the length of the photonic crystal waveguide. The slight wavelength dependence of the group index $n_g^{ref}(\lambda)$ in the reference arm was taken into account using exponential fitting of the theoretical black dashed curve in Fig. 2b as $n_g^{ref}(\lambda) = 1.2 \times 10^{-32}\exp(\lambda/21.32) + 4.06$. Blue circles in Fig. 2b represent the group index deduced from the transmission spectrum as described above, and exhibit group indices in excess of 300. The fringe visibility decreases towards the signal arm cut-off, which makes the assignment of transmission peaks to MZI-related interference fringes difficult. Detailed discussion of the limitations of the method is presented in Supplementary Information. In summary, the fringe amplitude and fringe spacing at these wavelengths becomes comparable with that of a superimposed residual Fabry–Perot (FP) noise with a similar amplitude (~1.5 dB) that arises from interference in the optical circuit outside the MZI. Fortunately, the main oscillation period of the FP noise (~0.15 nm) is almost constant throughout the spectrum, which corresponds to the distance of ~1 mm between the MZI and the input fibre couplers at the facets of the photonic chip. This allows even small fringes at wavelengths longer than 1,602 nm (shown in Fig. 2a inset) to be assigned as arising from the MZI. The last few data points around 1,602.65 nm correspond to very large group indices of over 500. However, the experimental error here is also large, since the fringe amplitude is approaching that of FP noise. The group index spectral dependence deviates from a smooth monotonically increasing theoretical curve calculated for infinitely long structures, and in turn also exhibits oscillations converging towards the photonic crystal mode cut-off (Fig. 2b inset). These oscillations can be readily attributed to

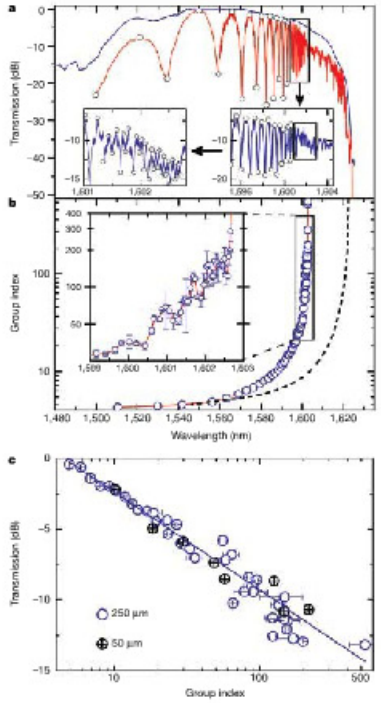

Figure 2 | Optical measurements of a passive unbalanced MZI. **a**, Transmission spectra of a straight photonic crystal waveguide with hole radii $0.251a$ and length 250 μm (black curve) and of a MZI (red curve) with 250-μm-long photonic crystal waveguides having hole radii $0.251a$ in the reference arm and $0.263a$ in the signal arm. Open blue circles represent spectral positions of the minima and maxima of the interference fringes used for calculation of the group index. The two insets show a consecutively magnified view of the spectrum near the transmission cut-off of the signal arm. **b**, Semi-logarithmic plot of the group index in the signal arm (open blue circles) extracted from the transmission spectrum. Inset shows the blown-up portion of the main plot near the transmission cut-off of the signal arm. Dashed black line shows the results of three-dimensional plane wave calculations of the group index in the reference arm. **c**, Amplitude of interference fringe maxima as a function of the group index for two MZI with photonic crystal waveguide lengths of 50 μm (crossed black circles) and 250 μm (open blue circles). Blue curve is a fitting with a power law dependence $T = a(n_g)^b$, where $a = 3.22$ and $b = -0.74$. The procedure for error determination is described in the Supplementary Discussion. The error bars are estimated from the maximum value of uncertainty in defining the spectral position of each individual extremum in transmission spectra.

Bloch–Floquet modes (or group delay ripples) in the finite-length photonic crystal waveguide[21].

To determine the potential of photonic crystal waveguides with large group indices in applications such as all-optical buffering, the chromatic dispersion and propagation losses need to be analysed. A strong increase of the group index close to the cut-off wavelength results in a sharp increase of the group velocity dispersion. This chromatic dispersion can be estimated from the results of Fig. 2b as 500 ps nm^{-1} mm^{-1} for group indices around 100. Compared with the chromatic dispersion in conventional telecommunications fibres, this is approximately 10^7 times higher. This induces significant broadening of ultrafast optical pulses transmitted through a photonic crystal waveguide, as observed in recent experiments[16]. Simple estimations show, however, that this extremely large dispersion might still allow operation of an all-optical buffer incorporating a millimetre-long photonic crystal waveguide that can store three bits of information at 10 Gbit s^{-1} data rate (ref. 10).

Propagation and coupling losses in the slow light regime can in principle result in the loss of stored information. The total loss in the photonic crystal waveguide as a function of the group index is analysed in Fig. 2c, where the amplitudes of the fringe maxima are shown (blue circles). Comparison with the results from another MZI device with five times shorter photonic crystal waveguides ($L = 50$ μm in each arm; black crossed circles in Fig. 2c) shows that propagation losses are virtually absent and that the fringe visibility is mainly affected by increasingly large coupling losses, which is in agreement with previously published data[19]. Thus further engineering of the coupling interface is essential to promote efficient coupling of light into the photonic crystal mode if even higher group indices (longer group delays) are to be accessed.

Slow light propagation can be exploited for a broader range of applications[9,10]—for example, variable optical buffers or dynamic dispersion compensators—if it can be tuned by external electrical signals. This can be done, for example, by passing an electric current between metallic contacts and thereby locally heating the signal arm of the MZI[22–25]. However, electrical contacts placed directly onto the silicon waveguide in the immediate vicinity of the strongly confined photonic crystal mode result in large absorption losses[22,23]. Increasing the distance between the photonic crystal mode and the contacts helps to minimize absorption, but requires larger electrical powers to change the refractive index[22,24,25]. Here we present a solution to this problem based on the idea of lateral electrical contacts to the photonic crystal, which itself acts as a micro-heater[26,27]. Figure 3a shows the magnetic field energy density profile of the photonic crystal mode calculated by the plane wave expansion method[20] for the slow light regime, showing that over 90% of the mode energy is confined within only 500 nm from the waveguide centre. Excellent optical isolation exceeding −50 dB is obtained with only four rows of holes on each side of the waveguide. Implementing this idea, ohmic lateral electrical contacts were defined on top of the photonic crystal

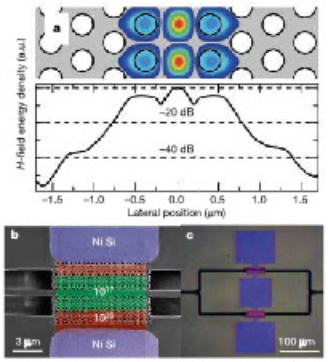

Figure 3 | Active electrically tunable MZI with lateral electrical contacts to photonic crystal waveguides. **a**, Time averaged magnetic field energy density calculated by the plane wave method in top-down view (false colour linear scale) and plotted on a semi-logarithmic scale (integrated over one unit cell). **b**, SEM image of the fabricated photonic crystal waveguide with lateral electrical contacts superimposed with a false colour representation to denote the different doping levels. **c**, Optical micrograph of the completed MZI circuit with three electrical contacts.

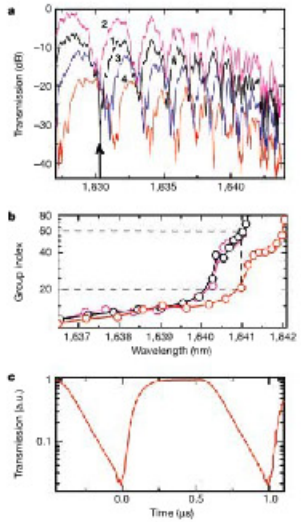

Figure 4 | Thermo-optic tuning of the group index in the active unbalanced MZI. **a**, Set of transmission spectra measured at the output of the MZI for different applied electric power. Spectra are shifted vertically by 5 dB for clarity. Spectrum 1 (black) corresponds to zero applied power. Spectrum 2 (magenta) was measured with 1.5 mW power applied to the reference arm, and is almost identical to spectrum 1 except for a slight shift of the fringes to shorter wavelengths. Spectrum 3 (blue) and spectrum 4 (red) were measured with 1 mW and 2 mW electric power, respectively, applied to the signal arm. A large shift of the fringes to longer wavelengths is evident. **b**, Semi-logarithmic plot of the group index dispersion extracted from the spectra in **a**. Black circles correspond to spectrum 1 with zero applied power. Magenta circles correspond to spectrum 3 with 1.5 mW applied to the reference arm. Red circles correspond to spectrum 4 with 2 mW power applied to the signal arm. **c**, Time response of the MZI with a 1 MHz square-wave modulated electric signal corresponding to 2 mW electrical power applied to the signal arm. The wavelength of the laser is tuned to 1,630 nm, as shown by the arrow in **a**.

waveguide separated by 1.5 μm from the waveguide core, as shown in Fig. 3b. Details of the design and fabrication are presented in Methods and Supplementary Information. Three contacts to the MZI device were formed as shown in Fig. 3c, which allows both the signal and reference arms to be addressed independently.

Transmission spectra for an unbalanced active MZI are presented in Fig. 4a. Owing to different structural parameters of the active MZI, the cut-offs of the signal and reference arms occur at around 1,642 nm and 1,655 nm, respectively. Measurements are shown for different electric power levels applied consecutively to the signal and reference arms. Using the procedure described above, the group index of the signal arm can be deduced from the spectral positions of the interference fringes. Figure 4b represents three typical measurements of the group indices of the signal arm with and without applied electric power. Local heating of the signal arm results in the wavelength shift of the group index dispersion curve to longer wavelengths. For a given wavelength, for example 1,641 nm, the group index is tuned from 20 to 60 with 2 mW of electric power applied to the signal arm (red curve in Fig. 4b). An even larger tuning range can be achieved at longer wavelengths. But because the active MZI device underwent nine additional fabrication steps (see Supplementary Information), the amplitude of residual FP noise is increased, which prevents accurate measurements of group indices higher than 80. As expected, heating of the reference arm (with its group index nearly constant throughout this spectral region) does not result in significant changes of the measured group index dispersion (magenta curve in Fig. 4b).

In order to measure the time response of the active MZI device, the laser was tuned to 1,630 nm wavelength, where the application of 2 mW power to the signal arm results in almost π phase shift, as is evident from corresponding spectra in Fig. 4a (black and red curves). Transmission through the MZI is switched from the opaque state (fringe minimum in the black spectrum in Fig. 4a) to almost complete transmission (fringe maximum in the red spectrum in Fig. 4a) within only 100 ns, as is seen from Fig. 4c. This time response is the fastest yet reported for thermo-optic modulators[23–25], and is a direct result of the deep scaling of the device size. In our device, the heat generation and dissipation is localized to a very small volume in the silicon photonic crystal membrane (estimated as only 400 μm^3).

METHODS

Design and fabrication of the unbalanced passive photonic crystal MZI. Photonic crystal (PhC) structures were fabricated on 10 Ω·cm p-type silicon-on-insulator 200 mm wafers from SOITEC with a 2 μm buried oxide layer (BOX) and a thin silicon layer (thickness d = 223 nm) on a standard CMOS fabrication line as described elsewhere[11,14]. PhCs with a triangular lattice of holes with a period a = 437 nm were defined by etching holes with radius $R \approx 0.25a$ (109 nm) through a silicon layer. Note that to create an unbalanced MZI, the PhC waveguide in the reference arm and signal arm have holes of radius $0.251a$ and $0.265a$, respectively. PhC waveguides were formed by omitting one row of holes in the lattice along the Γ–K direction, as shown in Fig. 1a. After etching the silicon, the BOX was selectively etched away in the PhC waveguide region leaving a suspended silicon membrane perforated with holes (Fig. 1b). PhC waveguides with these parameters are known to possess a very broad bandwidth, with the low loss single-mode propagation extending from 1,520 nm to 1,620 nm with losses measured as small as 8 ± 2 dB cm^{-1} (ref. 12). Access strip waveguides with 460 nm width are butt-coupled to the PhC waveguides through a lateral taper with the final width of 757 nm corresponding to $\sqrt{3}a$ (ref. 11), which closely matches the geometrical spread of the modes. In order to reduce the coupling losses arising from strong mode impedance mismatch at the coupling interface[14], the PhC lattice was terminated at the position of the cut going through the centre of the holes nearest to the waveguide, as shown in Fig. 1a. Utilization of efficient ultra-compact 15° angle Y-splitters and 90° bends with radius R = 5 μm (ref. 28) (see Fig. 1b, c) allows not only the footprint of the MZI device to be shrunk to 0.04 mm^2, but also allows very low insertion losses through the MZI; below 1 dB over a wide bandwidth, as evident from Fig. 2a. In principle, the device footprint can be easily scaled down to 0.01 mm^2 and is currently limited by a necessity to place large electric contacts inside the MZI for easy electric probing. In order to couple light from a fibre to the photonic chip, the access strip waveguides were terminated at the input and output with polymer fibre couplers based on an inverted taper design, as reported in ref. 11.

Design and fabrication of an electrically tunable PhC MZI. Active MZI devices were created by adding lateral electrical contacts to the PhC waveguide. Ohmic contacts were formed by p-doping the outer edge of the PhC region and contact pad regions outside the MZI with boron ions to 10^{20} cm^3 concentration, as shown in Fig. 3b. Metal contacts were formed in the same region by nickel deposition and subsequent silicidation. In order to decrease the device impedance, the central core of the PhC waveguide was also doped, to a concentration of only 10^{17} cm^3. This provides impedances in the 10 kΩ range while increasing the insertion loss by only 2 dB, as measured from corresponding transmission spectra in Fig. 4a. Fabrication of the finished MZI device requires six levels of lithography. A detailed description and schematic of the fabrication sequence is presented in Supplementary Information.

Measurements of transmission spectra. TE-polarized (electric field in the silicon slab plane) transmission spectra were measured with two complementary set-ups. The first utilizes a broad band light source covering the 1,200–1700 nm wavelength region (Agilent 83437B), and spectra were recorded with an optical spectrum analyser (Agilent 86140B) with 60 pm resolution (blue curve in Fig. 2a and all spectra in Fig. 4a). The second set-up uses solid state lasers (New Focus, Velocity 6328H, 6330), tunable in 0.12 pm steps in the 1,500 nm–1,632 nm wavelength range (red spectra in Fig. 2a). The narrow linewidth of the laser (100 MHz) corresponds to a coherence length that exceeds all characteristic optical lengths in the measurement system, and allows accurate resolution of interference fringes with a free spectral range below 0.01 nm. The light sources are coupled to a polarization maintaining (PM) fibre and are passed to the polarization controller. Coupling to/from the photonic chip is provided via micro-lensed and tapered PM fibres aligned with the input/output on-chip polymer fibre couplers using xyz piezo-translational stages[11,14]. Efficient coupling (<0.5 dB loss per port[11]) allows the mean amplitude of the Fabry–Perot noise to be minimized to only 1.5 dB. A rejection ratio of over 30 dB between TE and TM polarizations is achieved. The transmission spectra of the PhC waveguides and the MZI devices were normalized to the transmission spectra of corresponding single-mode reference strip waveguides[11] located in the same writing field near the PhC structures[11].

Numerical simulations. To obtain the dispersion of the group index, the photonic band structure was calculated with a three-dimensional full-vector plane wave expansion method using the MIT Photonics Band software code[19]. The dielectric permittivity of the Si slab was taken as 12.1. Values for the hole radii, lattice constant and slab thickness were taken from the scanning electron microscope (SEM) measurements. The grid resolution (number of vectors in the unit cell of the PhC) of the plane wave calculations was set to 16 × 16 × 16, which gives an error in the eigenvalue convergence below ~2% with reasonable calculation time.

Received 5 April; accepted 6 September 2005.

1. Brillouin, L. *Wave Propagation and Group Velocity* (Academic, New York, 1960).
2. Hau, L. V. *et al.* Light speed reduction to 17 metres per second in an ultracold atomic gas. *Nature* **397**, 594–598 (1999).
3. Liu, C. *et al.* Observation of coherent optical information storage in an atomic medium using halted light pulses. *Nature* **409**, 490–493 (2001).
4. Bajcsy, M. *et al.* Stationary pulses of light in an atomic medium. *Nature* **426**, 638–641 (2003).
5. Lukin, M. D. & Imamoglu, A. Controlling photons using electromagnetically induced transparency. *Nature* **413**, 273–276 (2001).
6. Ku, P. C. *et al.* Slow light in semiconductor quantum wells. *Opt. Lett.* **29**, 2291–2293 (2004).
7. Turukhin, A. V. *et al.* Observation of ultraslow and stored light pulses in a solid. *Phys. Rev. Lett.* **88**, 023602 (2002).
8. Bigelow, M. S. *et al.* Superluminal and slow light propagation in a room-temperature solid. *Science* **301**, 200–202 (2003).
9. Mok, J. T. & Eggleton, B. J. Expect more delays. *Nature* **433**, 811–812 (2005).
10. Khurgin, J. B. Optical buffers based on slow light in electromagnetically induced transparent media and coupled resonator structures: comparative analysis. *J. Opt. Soc. Am. B* **22**, 1062–1074 (2005).
11. McNab, S. J., Moll, N. & Vlasov, Y. A. Ultra-low loss photonic integrated circuit with membrane-type photonic crystal waveguides. *Opt. Express* **11**, 2927–2939 (2003).
12. Dulkeith, E., McNab, S. J. & Vlasov, Y. A. Mapping the optical properties of slab-type two-dimensional photonic crystal waveguides. *Phys. Rev. B* **72**, 115102 (2005).
13. Krauss, T. F., De La Rue, R. & Brand, S. Two-dimensional photonic-bandgap structures operating at near-infrared wavelengths. *Nature* **383**, 699–702 (1996).
14. Notomi, M. *et al.* Extremely large group-velocity dispersion of line-defect waveguides in photonic crystal slabs. *Phys. Rev. Lett.* **87**, 253902 (2001).

15. Vlasov, Y. A. *et al.* Femtosecond measurements of the time of flight of photons in a three-dimensional photonic crystal. *Phys. Rev. E* **60**, 1030–1035 (1999).
16. Gersen, H. *et al.* Real-space observation of ultraslow light in photonic crystal waveguides. *Phys. Rev. Lett.* **94**, 073903 (2005).
17. Astratov, V. N. *et al.* Heavy photon dispersions in photonic crystal waveguides. *Appl. Phys. Lett.* **77**, 178–180 (2000).
18. Altug, H. & Vuckovic, J. Experimental demonstration of the slow group velocity of light in two-dimensional coupled photonic crystal microcavity arrays. *Appl. Phys. Lett.* **86**, 111102 (2004).
19. Vlasov, Y. A. & McNab, S. J. Coupling into the slow light mode in slab-type photonic crystal waveguides. *Opt. Lett.* (in the press); preprint at (http://arxiv.org/abs/physics/0504102) (2005).
20. Johnson, S. G. & Joannopoulos, J. D. Block-iterative frequency-domain methods for Maxwell's equations in a planewave basis. *Opt. Express* **8**, 173–190 (2001).
21. Bendickson, J. M., Dowling, J. P. & Scalora, M. Analytic expressions for the electromagnetic mode density in finite, one-dimensional, photonic band-gap structures. *Phys. Rev. E* **53**, 4107–4121 (1996).
22. Cocorullo, G. & Rendina, I. Thermo-optical modulation at 1.5μm in silicon etalon. *Electron. Lett.* **28**, 83–85 (1992).
23. Geis, M. W., Spector, S. J., Williamson, R. C. & Lyszczarz, T. M. Submicrosecond submilliwatt silicon-on-insulator thermooptic switch. *IEEE Photon. Technol. Lett.* **16**, 2514–2516 (2004).
24. Espinola, R. L., Tsai, M.-C., Yardley, J. T. & Osgood, R. M. Fast and low-power thermooptic switch on thin silicon-on-insulator. *IEEE Photon. Technol. Lett.* **15**, 1366–1368 (2003).
25. Camargo, E. A., Chong, H. M. H. & De La Rue, R. M. 2D Photonic crystal thermo-optic switch based on AlGaAs/GaAs epitaxial structure. *Opt. Express* **12**, 588–592 (2004).
26. McNab, S. J., Hamann, H. F., Vlasov, Y. A. Lateral electrical contacts for photonic crystal based integrated opto-electronic devices. Pending US patent US20050084195A1 (15 October 2003).
27. McNab, S. J., Hamann, H. F., O'Boyle, M. & Vlasov, Y. A. Method and apparatus for thermo-optic modulation of optical signals. Pending US patent, US20050084213A1 (12 January 2004).
28. Vlasov, Y. A. & McNab, S. J. Losses in single-mode silicon-on-insulator strip waveguides and bends. *Opt. Express* **12**, 1622–1631 (2004).

Supplementary Information is linked to the online version of the paper at www.nature.com/nature.

Acknowledgements This work was partially supported by the DARPA DSO Slow Light programme.

 Correspondence and requests for materials should be addressed to Y.A.V. (yvlasov@us.ibm.com).